Cell Motility and Local Viscoelasticity of Fibroblasts

S. Park,* D. Koch,§ R. Cardenas,* J. Käs,§ and C. K. Shih*†‡
*Department of Physics, †Texas Materials Institute, and ‡Center for Nano and Molecular Science, University of Texas, Austin, Texas 78712; and §Fakultät für Physik und Geowissenschaften, Universität Leipzig, D-04103 Leipzig, Germany

ABSTRACT Viscoelastic changes of the lamellipodial actin cytoskeleton are a fundamental element of cell motility. Thus, the correlation between the local viscoelastic properties of the lamellipodium (including the transitional region to the cell body) and the speed of lamellipodial extension is studied for normal and malignantly transformed fibroblasts. Using our atomic force microscopy-based microrheology technique, we found different mechanical properties between the lamellipodia of malignantly transformed fibroblasts (H-ras transformed and SV-T2 fibroblasts) and normal fibroblasts (BALB 3T3 fibroblasts). The average elastic constants, K, in the leading edge of SV-T2 fibroblasts (0.48 $\pm$ 0.51 kPa) and of H-ras transformed fibroblasts (0.42 $\pm$ 0.35 kPa) are significantly lower than that of BALB 3T3 fibroblasts (1.01 $\pm$ 0.40 kPa). The analysis of time-lapse phase contrast images shows that the decrease in the elastic constant, K, for malignantly transformed fibroblasts is correlated with the enhanced motility of the lamellipodium. The measured mean speeds are 6.1 $\pm$ 4.5 μ m/h for BALB 3T3 fibroblasts, 13.1 $\pm$ 5.2 μm/h for SV-T2 fibroblasts, and 26.2 $\pm$ 11.5 μm/h for H-ras fibroblasts. Furthermore, the elastic constant, K, increases toward the cell body in many instances which coincide with an increase in actin filament density toward the cell body. The correlation between the enhanced motility and the decrease in viscoelastic moduli supports the Elastic Brownian Ratchet model for driving lamellipodia extension.

INTRODUCTION

The cytoskeleton is a three-dimensional polymer scaffold which spans the cytoplasm of eukaryotic cells. This network is mainly composed of actin filaments, microtubules, intermediate filaments, and accessory proteins. In lamellipodia, actin filaments are predominantly found and serve as a key structural element. In addition, f-actin acts as a polymeric machine, which generates the protrusive force for an advancing cell. Thus, the actin cytoskeleton affects cell motility as well as a cell's viscoelastic properties. Previous studies can be roughly divided into two groups, those focusing on the actin cytoskeleton as a governing element of cell motility (1–5) and those concentrating on how alterations of cytoskeleton result in changes in the viscoelastic properties (6–9). Nevertheless, very few studies focused on the correlation between a cell's viscoelastic properties and motility, which are both affected by the actin cytoskeleton. Moreover, the thinness of the lamellipodium of a cell ($<$1000 nm) has hindered accurate measurements of its viscoelastic properties (10).

From a mesoscopic point of view, an important component of a cell's motion, such as the amoeboid movement, is manifested by a gel-sol transition (11). Some investigators have suggested a similar mesoscopic mechanism to explain the motility of *Listeria* (12). However, there is very little understanding of how the mesoscopic signature is related to the microscopic mechanism. For example, it is not clear how the viscoelastic change of the lamellipodium is related to the polymerization of actin filaments for a cell's motility. Thus, the ability to probe a cell's local viscoelastic properties with a high spatial resolution should advance our understanding of the cytoskeletal machinery that governs cell motility and cellular stiffness.

Several models have been proposed to explain the mechanism of force generation for a cell's movement at the molecular level. Many models are based on the fact that the actin polymerization is a major contributor to the protrusive force, which leads to the extension of the lamellipodia of crawling cells on a hard substrate. The Brownian ratchet model was proposed to explain how polymerizing filaments could rectify the Brownian motion of an object to produce a unidirectional force (13). The finding that *Listeria* and *Shigella* display the same movement speed despite having a big difference in their Brownian motion forces the model to be amended to the elastic Brownian ratchet model (14,15). In that model, the bending motion of elastic filaments allows intercalation of actin monomers to push a cell forward. It successfully explains the force generation of the orthogonal actin network observed in lamellipodia (16). For the bacterial movements, Marcy et al. suggest a different model, which describes the bacteria as a rigidly attached actin tail on a coated polystyrene bead (17).

Another model, the so-called dendritic nucleation model, is also based on actin polymerization: treadmilling of a branched actin network is mainly responsible for the protrusion of the lamellipodium (18). Mullins et al. reported that the Arp2/3 complex controls the formation of a branched network of actin filaments at the lamellipodium. The presence of actin-depolymerizing factor/cofilin (known to promote filament

Submitted September 25, 2004, and accepted for publication September 15, 2005.

Address reprint requests to Soyeun Park at her present address, Dept. of Biomedical Engineering, University of Texas, Austin, TX 78712. E-mail: sypark20@physics.utexas.edu.

0006-3495/05/12/4330/13 $2.00

doi: 10.1529/biophysj.104.053462

disassembly) at the rear of the lamellipodium provides an additional support for this model (19).

Another group of models is based on myosins, a family of molecular motors specific to actin filaments. Studies have been performed to investigate whether any myosin is required for the protrusion of nonmuscle cells. It was found that *Dictyostelium*, whose myosin heavy chains were genetically disrupted, could display normal protrusions (20,21). However, some investigators reported that *Dictyostelium*, which lacks unconventional myosin encoded by the Myo A gene, exhibited impairments in pseudopod extension (22,23). Thus far, these studies have failed to provide consistent evidence that myosin leads to protrusion of the lamellipodium.

These different potential mechanisms for the protrusion of lamellipodia predict distinctively dissimilar behaviors in the correlation between the elastic modulus and motility. Some predict the correlation of low elastic moduli in the lamellipodial region with an enhanced motility, whereas others predict just the opposite. Therefore, quantitative studies of the local viscoelastic properties and their correlation with well-investigated parameters of cell motility play a crucial role in gaining insights into the fundamental mechanism.

Here, we report on quantitative studies of the local viscoelastic properties and their correlation with the motility and f-actin content of normal and malignantly transformed fibroblasts. Malignant transformation is known to induce morphological alterations in the cytoskeleton, leading to changes in a cell's viscoelastic properties (24,25). Moreover, malignantly transformed fibroblasts are known to display enhanced motility, which has been attributed to the invasive and metastatic ability (26,27).

The local viscoelastic properties are measured using an atomic force microscopy (AFM)-based microrheological method (28). The AFM has the advantage of nanoscale force measurements in a localized region (29–33). Especially, our spherical probe provides a controlled nondestructive stress (100 Pa–10 kPa) for biological samples and allows the application of the Hertz model to determine the viscoelastic moduli. More recently, we extended the method by applying two additional models that consider substrate effects and high strains in the thin lamellipodial regions (34): the Chen model for well-adhered regions and the Tu model for non-adhered regions (35–37). Furthermore, both models were extended to deal with frequency-dependent viscoelastic contributions.

For the cell motility, we acquired time-lapse images using phase contrast microscopy. Adhering to previous cell motility studies, time variation of a center of area enclosed by the perimeter of a cell is used to calculate the mean speed of a cell (38,39). In addition, we determined the cell's extending ability by tracking the area changes of the lamellipodium.

As a result, we observe a reduced viscoelastic modulus and an enhanced motility in the malignantly transformed fibroblasts compared with the normal fibroblasts. We find that the lamellipodium of a fibroblast has a reduced elastic modulus compared with the regions close to the cell body. This reduction is more pronounced for the malignantly transformed fibroblasts, which are more motile. This result demonstrates the correlation between the enhanced motility and the decrease in viscoelastic moduli. This correlation can be understood by an elastic Brownian ratchet model (14). More specifically, an increase in thermal fluctuations of actin filaments in the softer cells and the lamellipodium can expedite the intercalation of G-actin that leads to the enhanced protrusion.

MATERIALS AND METHODS

Cells

The data were taken from normal (BALB 3T3) and malignantly transformed fibroblasts (H-ras transformed and SV-T2 fibroblasts) obtained from American Type Culture Collection (Manassas, VA). The cells were cultured with Dulbecco's modified Eagle's medium (DMEM; American Type Culture Collection), supplemented with 10% calf serum (American Type Culture Collection). For H-ras transformed fibroblasts, calf serum was substituted by fetal bovine serum (American Type Culture Collection). Before measurements, cells were incubated at 37°C in 5% CO_2 atmosphere.

For AFM experiments, the cells were plated on presterilized coverslips a day before data were taken. To keep the pH constant (~7.4) during AFM measurements, 10 mM HEPES (Sigma Aldrich, St. Louis, MO) was added to the medium. Throughout the measurement, small amounts of the temperature-controlled medium were continuously provided through the inlet of the liquid cell (Microcell, TM Microscopes, Sunnyvale, CA). To ensure the viability of the investigated cells, all measurements were taken within 2 h after removing the cells from the incubator.

For the motility experiments, the cells were plated on our presterilized customized sample chamber shown in Fig. 1 *A* a day before data were taken.

AFM measurements

All AFM measurements were performed using a commercial atomic force microscope (Autoprobe CP, Park Scientific Instruments, Woodbury, NY). We used commercial cantilevers (Microlevers, TM Microscopes, Woodbury, NY). To obtain a well-defined spherical probe shape, we glued a polystyrene bead (Seradyn Particle Technology, Indianapolis, IN) at the end of the AFM tip using standard transmission electron microscope epoxy with a low viscosity (M-Bond 610, SPI Supplies, West Chester, PA). The cleanness and the radius of a probe (1.5–4 μm) were investigated through its topographic AFM image. The force constant of each cantilever (0.02–0.06 N/m) was obtained by calibrating against a cantilever with a known force constant. The calibration cantilever was obtained when the force constants from three different calibration methods agreed within 5% (40,41). These three procedures involved the calibration method with a commercial cantilever of known force constant (0.157 N/m) (TM Microscopes), the thermal fluctuations method, and the resonance frequency method.

The force curves were acquired with a 1 s time interval, i.e., 1 Hz. This allowed us to calculate the zero-frequency elastic constants, K. The frequency-dependent viscoelastic moduli were obtained by superimposing the sinusoidal oscillations (amplitude of 5–20 nm and frequency of 50–300 Hz) on the scanner movements while taking the force curves. The experimental details are described in our previous publication (28).

Phase contrast microscopy

We investigated the crawling movements of cells on coverslips under the inverted phase contrast microscope (Zeiss, Axiovert 100M, Jena, Germany)

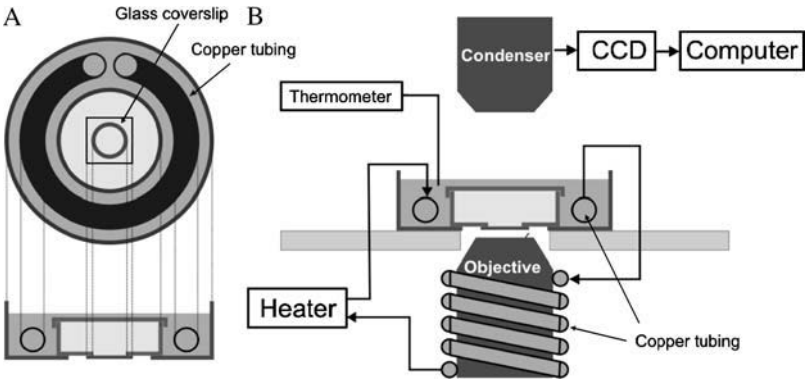

FIGURE 1 Setup for the experiments of cell motility. (*A*) The schematic diagram of the phase contrast microscope equipped with the charge-coupled device camera and the custom-built temperature control system. The warm water from the heater constantly flows through the copper tubing to control the temperature throughout the experiments. (*B*) The drawing of our sample chamber. The sample chamber consists of two compartments: an inner and outer chamber. The cells were placed on the coverslips glued on the bottom of the inner compartment, and the copper tubing for the temperature control was placed in the outer compartment and around the objective.

with a 63× oil immersion objective (Zeiss, Plan Neofluar, Antiflex, Ph3, numerical aperture = 1.25). The schematic diagram of the setup is shown in Fig. 1 *B*. Time-lapse images of the investigated cells were recorded through a high resolution and low light charge-coupled device camera (Orca100, Hamamatsu Photonics, Hamamatsu City, Japan) mounted on the microscope. We used commercial software (Axiovision, Zeiss) to capture images with a 1-min time interval for 30 min. Since we had an interest in the extension and retraction of the lamellipodium, we stopped recording the images when the investigated cell detached its tail from the substrate or overlapped with other cells since the tail detachment involves different mechanical actions compared with the lamellipodium remodeling. We stopped the measurements ~6 h after removing the cells from the incubator to ensure cells' normal physiological condition.

Fluorescence microscopy

For the histochemical staining, cells were fixed for 10 min with 0.3% glutaraldehyde in Brinkley Buffer (BRB80) and washed with phosphate-buffered saline (PBS). Subsequently, cells were permeabilized with 0.1% Triton-X (Sigma Aldrich) in PBS at 4°C. To visualize the actin filaments, cells were stained with 0.2% TRITC-phalloidin (Sigma Aldrich) in PBS for 30 min at room temperature and then washed with PBS. Fluorescence images were taken with a confocal laser scanning microscope (TCS SP2 AOBS, Leica Microsystems, Bensheim, Germany). Final fluorescence images were calculated from stacked image series in the vertical direction through a cell with 4× line average and a step of ~500 nm, which were obtained using a 63× oil immersion objective (Leica Microsystems, PL APO, numerical aperture = 1.4).

To delineate a spatial profile of the actin filaments, the average actin fluorescence intensity at each pixel was obtained. Pixels in thin regions such as the lamellipodium included values from regions outside of the cell. These values resulted in a very low intensity and led to a lower average intensity in these regions. To avoid this artifact, we excluded the values below the threshold intensity from the average calculation.

DATA ANALYSIS

Zero frequency elastic modulus

To calculate the indentation, δ, the contact point was determined as the point at which the slope of the force curve initially deviates from zero. Once we calculated the indentation, δ, and the deforming force, f_{bead}, applied on the probe, we used the Hertz model to determine the elastic constant, $K_{\text{Hertz}} = E_{\text{Hertz}}/(1 - \nu^2)$, which depends on the elastic modulus, E_{Hertz}, and the Poisson ratio, ν. K_{Hertz} is determined over the range of indentations where K_{Hertz} remains nearly constant as would be expected for linear elasticity. However, in the thin regions such as the lamellipodium, the Hertz model is no longer valid due to the strong substrate effect. In these regions, the data are better analyzed with the Tu (K_{Tu}) or the Chen models (K_{Chen}), which are modified from the Hertz model by considering the boundary conditions of the hard substrate effect: the Chen model for well-adhered regions and the Tu model for nonadhered regions (33). For these models, the cell's height at the measurement point, h, was determined from the AFM topographic image. The inevitable slight indentation occurring in the contact mode imaging was extrapolated from the force curve and added to the height. All measurements were performed on uncoated glass coverslips, avoiding errors in the viscoelastic data due to a soft substrate. Thus, cells predominantly adhered, through unspecific interactions, to the glass substrate. The details for calculating K from the Hertz, Tu, and Chen models are described in our previous publication (34).

Frequency-dependent viscoelastic modulus

Unlike polymer samples, biological cells demonstrate viscous behaviors as well as elastic behaviors. For the viscoelastic modulus, the total indentation, δ, is the sum of the oscillating indentation, $\tilde{\delta}^*$, and the offset indentation, δ_0. In this case, the contact point is determined as the point at which the maximum change in the phase difference between the cantilever and scanner movements occurs. The cantilever before contact is subject to the hydrodynamic drag of the surrounding viscous medium leading to a constant phase difference close to 90°. Once the tip makes contact with the sample, the phase difference significantly decreases. This drag force was directly measured by monitoring the cantilever oscillation right before the tip makes contact with the sample and subtracted from the total oscillatory viscoelastic force measured by the lock-in amplifier.

The complex viscoelastic constant, K^*_{Hertz1} ($K' + iK''$), is obtained by expanding the deforming force, f_{bead}, with

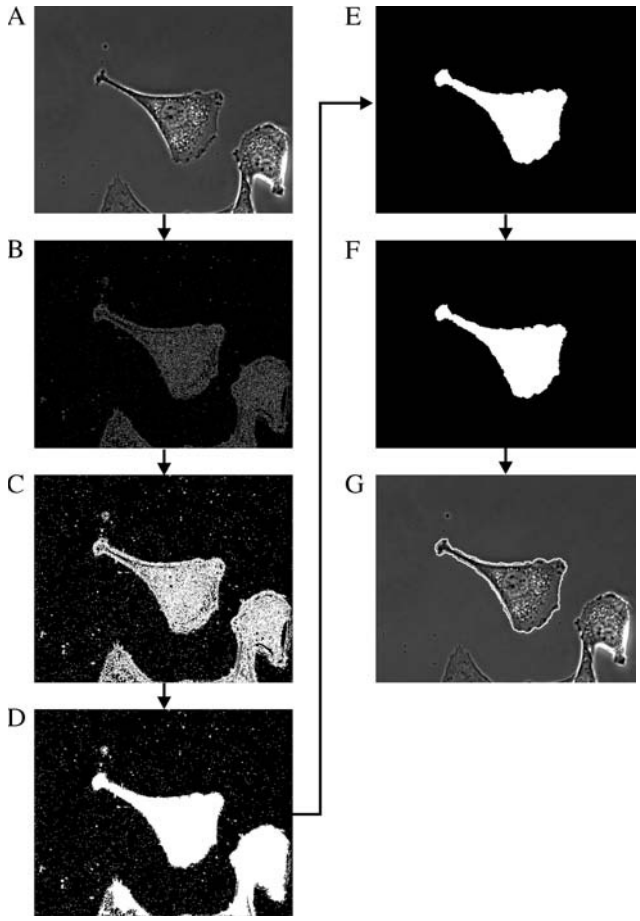

FIGURE 2 Steps in detecting the outlines of a cell using MATLAB. (*A*) The original image was taken from the phase contrast microscope. (*B*) The cell was segmented using a convolution method. (*C*) The gaps in the perimeter of the cell were dilated using linear structuring elements. (*D*) The holes in the interior of the cell were filled. (*E*) The objects beside the observed cell were removed. (*F*) The cell was smoothed by eroding the image. (*G*) The perimeter was placed around the cell.

respect to the indentation, δ, by a Taylor series. The real part, $K' = E'/(1-\nu^2)$, reflects the elastic (storage) constant and the imaginary part, $K'' = E''/(1-\nu^2)$, reflects the viscous (loss) constant of the sample. Here, E' and E'' represent the corresponding modulus. Analogous to the zero frequency measurements, in thin regions, the data are better analyzed with the Tu (K^*_{Tu1}) or the Chen model (K^*_{Chen1}). Detailed calculations for both models are described in our previous study (34).

Motility

We utilize the edge detection technique and the basic morphology tools provided by MATLAB to delineate a cell in time-lapse images. The convolution method was used to distinguish a cell from the background. Subsequent dilation using the linear structuring elements allows us to delineate the perimeter of the cell from the image (see Fig. 2).

We define the centroid as the geometric center of a cell. Assuming that each point enclosed by the perimeter of a cell is equally loaded, the centroid is calculated as the center of mass. Perimeters and centroids were obtained every 5 min for 30 min. The net path length was measured as a change of the centroid for each 5-min interval, $l_{5\mathrm{min}}$, and the 30-min total observation time, l. Since images were taken with the 5-min interval, in which cells visibly moved, errors due to the fact that the centroid is not a material point of the cell are insignificant. The mean speed, v, was determined from the net path length, l. The total path length, L, was also calculated by summing the net path length from each 5-min interval, $\sum l_{5\mathrm{min}}$. To understand how consistently a cell stays on a course, we define the directionality, D, as the ratio, l/L. Detailed explanations for tracking methods of the cell motility are described in the previous study (38).

In addition, we observed the change in area of the lamellipodium for 30 min. This observation reveals a cell's ability to remodel its lamellipodium to spur its movements. We chose, in the initial image, an arbitrary boundary of the lamellipodial region defined as one-third of the total distance from the leading edge to the nucleus (see the *rectangular box* in Fig. 3). This initial boundary was applied throughout the time-lapse images during the observed time. From the superimposed time-lapse images, we calculated a sum of the advanced forward and retracted areas (see Fig. 3). The activity of the lamellipodium, A, is defined as this sum divided by the initial area ($t = 0$) and the observation period. The normalization was necessary to allow the comparison between cells of different size.

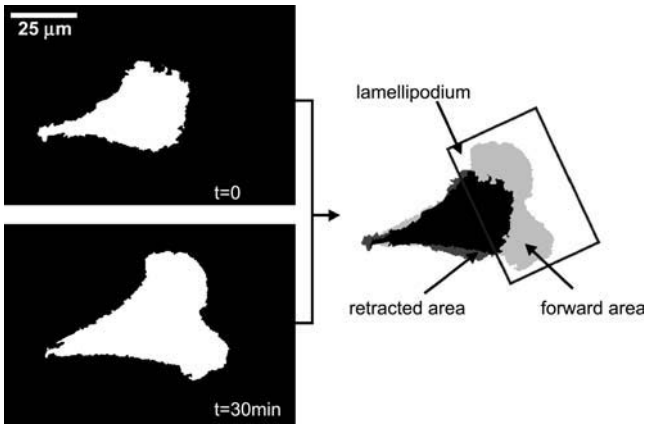

FIGURE 3 Advanced forward and retracted areas indicated in the overlapped images of an SV-T2 fibroblast taken with a 30-min time interval. For the lamellipodium (the area enclosed by the *rectangular box*), the area changes are calculated as a sum of the advanced forward and retracted areas. After normalizing them by the initial area ($t = 0$), the activity, A, is obtained by dividing the normalized area change by the time interval.

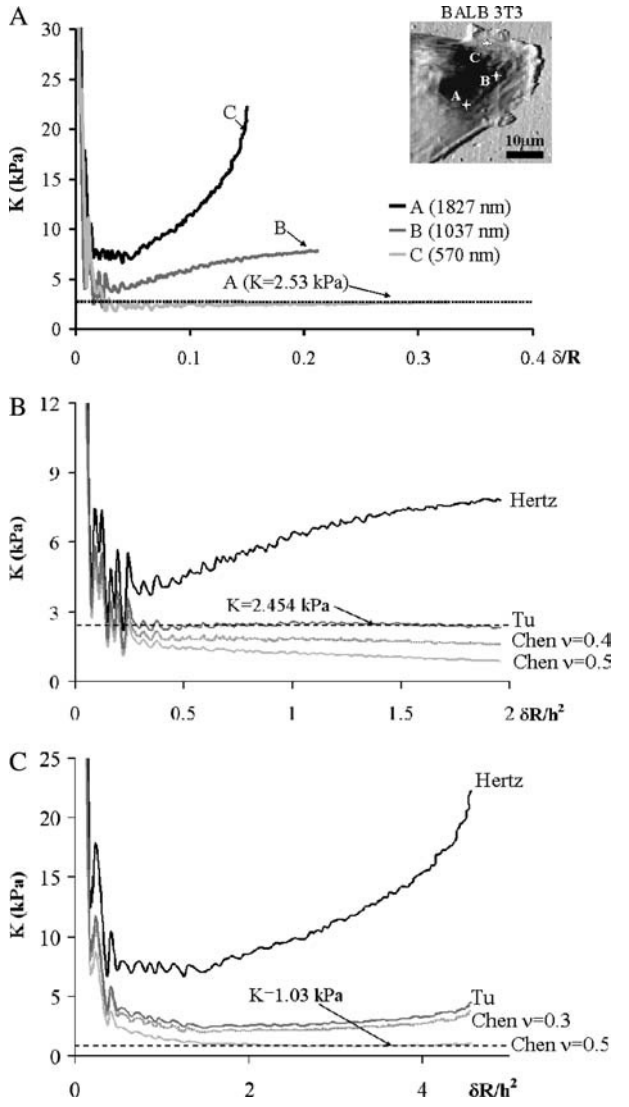

FIGURE 4 Elastic constant, K, obtained from a BALB 3T3 fibroblast. (*A*) The elastic constant, K, calculated from the Hertz model, plotted as a function of δ/R. Here, δ is the indentation and R is the radius of the probe. The data were taken at three different points on the BALB 3T3 fibroblast. The measurement points are indicated by the stars in the error mode image of the fibroblast. The height of each point is shown as well. The Hertz model yields a reasonable elastic constant for the data taken at point *A*. (*B*) The elastic constant, K, obtained at point *B* versus $\delta R/h^2$ as calculated from the Hertz, Tu, and Chen models with the various Poisson ratios, ν. Here, h is the height of the cell at the measurement point. The best result is obtained with the Tu model. (*C*) The elastic constant, K, obtained at point *C* versus $\delta R/h^2$ as calculated from the Hertz, Tu, and Chen models with the various Poisson ratios, ν. The best result is obtained with the Chen model with the Poisson ratio of 0.5.

Statistical analysis

All the data are presented as mean ± SD. For statistical comparisons of the data from three different cell lines, an ANOVA test with post hoc comparisons (Tukey's honestly significant differences test) was performed. Statistical significance was accepted for $p < 0.05$. In the figures, the standard deviations are plotted as error bars and * indicates the significant difference among the cell lines.

RESULTS

Lower viscoelastic moduli induced by malignant transformation

The elastic constants, K, were measured at ~3 different points on each fibroblast. Typical data obtained from the three cell lines are shown in Figs. 4–6. The elastic constant in the thicker cellular regions closer to the cell body is successfully obtained by the Hertz model (see *point A* in Figs. 4–6). However, due to the strong substrate effect, the data obtained from thin regions closer to the leading edge are reanalyzed with the Tu or the Chen model (see *points B* and *C* in Figs. 4–6). The average elastic constants, K, are plotted in Fig. 7 *A*.

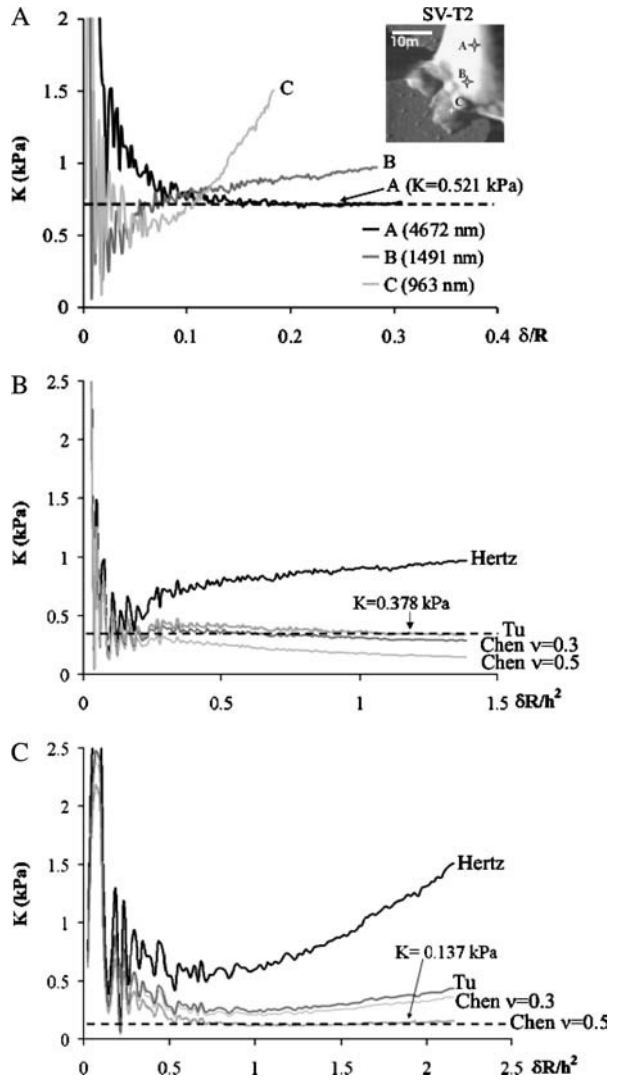

FIGURE 5 Elastic constant, K, obtained from an SV-T2 fibroblast, presented in the same format as Fig. 4.

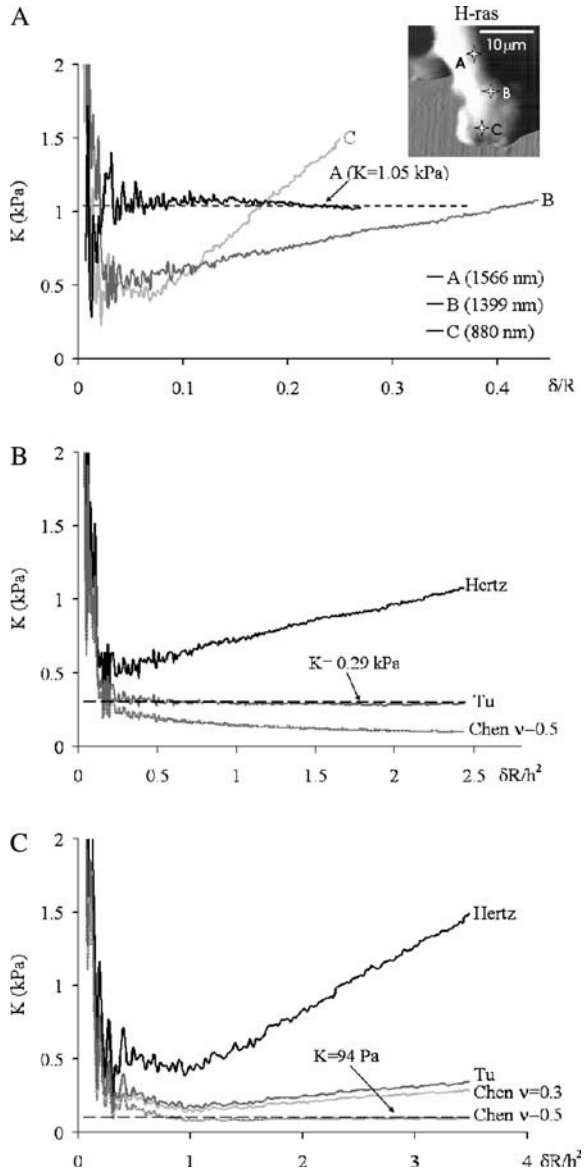

FIGURE 6 Elastic constant, K, obtained from an H-*ras* transformed fibroblast, presented in the same format as Fig. 4.

The average elastic constant in the leading edge, which excludes the repeated measurements on one cell, is provided in the gray column. There is a significant difference in the elastic constants between normal (1.01 ± 0.40 kPa) and malignantly transformed fibroblasts, whereas there is no significant difference between SV-T2 (0.48 ± 0.51 kPa) and H-ras transformed fibroblasts (0.42 ± 0.35 kPa). In addition, all of the elastic constants, K, including repeated measurements on one cell, are plotted as a histogram of occurrences (see Fig. 7 *B*). A wide distribution of elastic constants, K, from all three cell lines is observed. The normal fibroblasts display much wider distribution of K (0.34−4.95 kPa) than the malignantly transformed fibroblasts. Note that there is no occurrence of elastic constants exceeding 3.0 kPa for the malignantly transformed fibroblasts.

The decrease in the elastic constants, K, for malignantly transformed fibroblasts is also confirmed from the frequency-dependent measurements. Typical data obtained at 100 Hz are presented at Fig. 8. In thin regions, the frequency-dependent data were also best analyzed with the Tu or the Chen model with a Poisson ratio, ν, of 0.4 or 0.5. For all three cell lines, the storage moduli, K', are comparable to the elastic constants, K, obtained from our zero-frequency measurements. In Fig. 9, the storage, K', and loss constant, K'', obtained from each cell of the three cell lines are plotted as a function of the frequency.

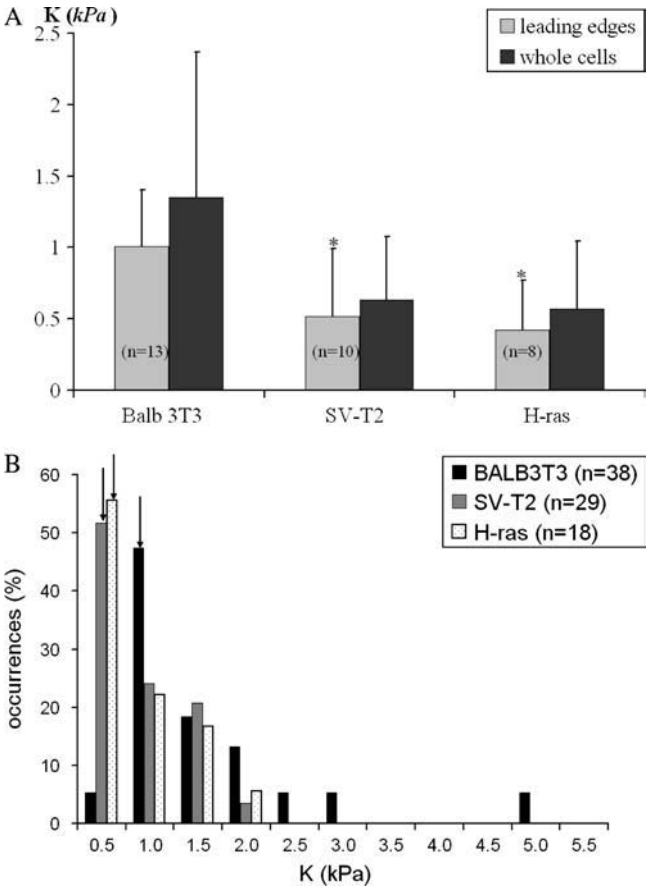

FIGURE 7 Elastic constant, K, from the three cell lines. (*A*) The average elastic constants, K. The gray columns represent the average elastic constants, K, in the leading edge. The number of measurements, n, represents the number of measured cells. The black columns represent the average elastic constants, K, including the repeated measurements on one cell. The repeated measurements were allowed at the different positions: 38 points from 13 BALB 3T3 fibroblasts, 29 points from 10 SV-T2 fibroblasts, and 18 points from 8 H-ras transformed fibroblasts. The statistical analyses were performed on the elastic constants, K, in the leading edge to avoid the complexity occurring from repeated measurements. The malignantly transformed fibroblasts display significant decreases compared with normal fibroblasts ($p < 0.05$). (*B*) The histogram of the elastic constants, K, including the repeated measurements on one cell. The arrows indicate the average elastic constants of each cell line. High elastic constants exceeding 3.5 kPa are obtained only from the BALB 3T3 fibroblasts.

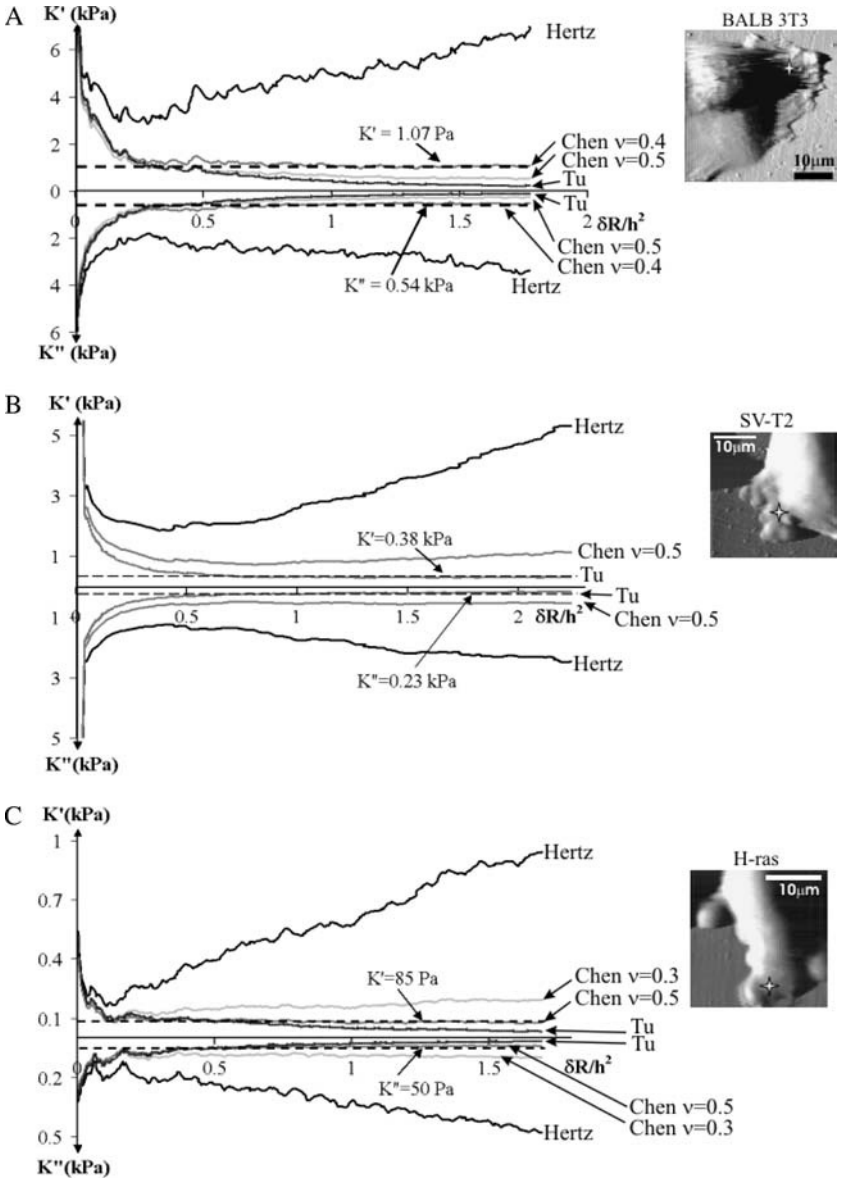

FIGURE 8 Storage, K', and loss constant, K'', at 100 Hz, plotted as a function of $\delta R/h^2$. The y axes represent positive values in both the upward and downward directions. The measurement points are marked by a star in the error mode image of each cell. The best results (indicated with the *dashed lines*) are obtained with the model indicated as below for each cell. (*A*) A BALB 3T3 fibroblast (the Chen model, $\nu = 0.4$). (*B*) A SV-T2 fibroblast (the Tu model). (*C*) An H-*ras* transformed fibroblast (the Chen model, $\nu = 0.5$).

Within the observed frequency range (50–300 Hz), all the cells display an elastic behavior characteristic of polymer gels in the rubber plateau regime, where the storage constant, K', exceeds the loss constant, K'' The observed elastic plateau regime was also found in previous measurements by both AFM and optical rheology (24,28,34). The malignantly transformed fibroblasts display a decrease in both the storage, K', and the loss constant, K'', compared with the normal fibroblasts within the observed frequency range.

Lower elastic moduli in lamellipodium

The local variation of the elastic constant, K, within a cell was investigated from the zero frequency elastic constants, K, measured at several points in the lamellipodium including the transitional region to the main body (see the *inset* of Fig. 10). The height served as a parameter of this local investigation since the height profile of fibroblasts placed on a hard substrate tends to increase from the lamellipodium to the cell body (570 nm–4700 nm). Fig. 10 shows the plots of the elastic constants, K, obtained from each cell from the three cell lines as a function of the height. These plots provide typical examples of the local profile of elastic constants, K, within a fibroblast that represents the dependency of the elastic constant on the sample height. In the leading edge, the observed fibroblasts in Fig. 10 show low elastic constants, which increase in regions toward the cell body.

However, some cases show that the elastic constants display the reverse behavior, i.e., the lamellipodium has a higher elastic constant, K, than the cell body. To clarify this point, we provide the distribution of fibroblasts, which display lower elastic constants in their lamellipodia (see Fig. 11). The major-

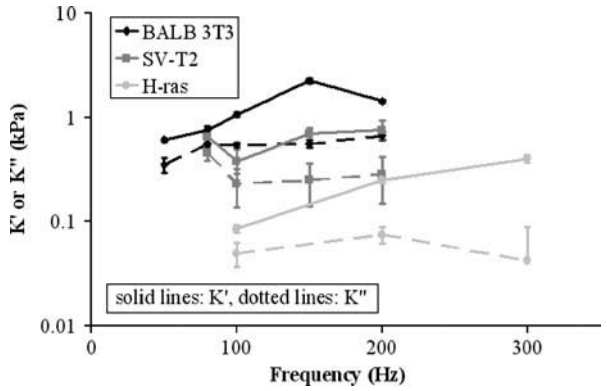

FIGURE 9 Storage, K', and loss constant, K'', plotted as a function of the frequency (50 Hz–300 Hz) for a BALB 3T3, an H-ras transformed, and an SV-T2 fibroblast. The storage (loss) constants, K' (K''), are shown by the solid (*dotted lines*). The data were taken at the same points indicated in the error mode image of the fibroblasts shown in the insets of Fig. 8. The data obtained from all the cell lines show that there is a partial rubber plateau region in the studied frequency range ($K' > K''$). The malignantly transformed fibroblasts show the significantly lower elastic plateau than the normal fibroblast.

ity of the forward moving fibroblasts during the AFM measurements display a decrease in the elastic constants in their lamellipodia. However, only a small portion of the retracting fibroblasts show lower elastic constants in their lamellipodia. Furthermore, a higher fraction of malignantly transformed fibroblasts shows a decrease in the elastic constants in the lamellipodium compared with normal fibroblasts.

Enhanced motility in malignantly transformed fibroblasts

Fig. 12 displays a typical example of the increase in motility of malignantly transformed fibroblasts compared with normal

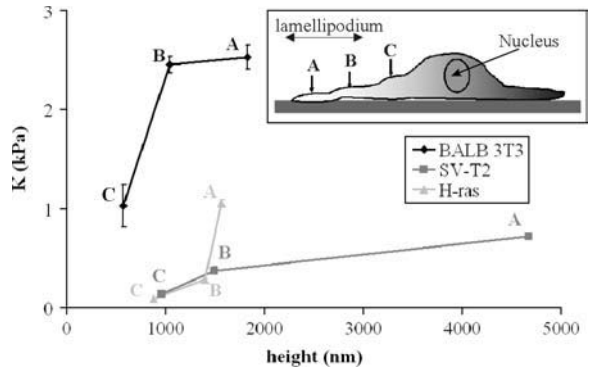

FIGURE 10 Zero frequency elastic constant, K, as a function of the height of the measurement point, h. The schematic drawing in the inset describes the representative points of A, B, and C, which locate the region from the leading edge toward the cell body. The data are obtained from the same points indicated in the insets of Figs. 4–6, respectively. The normal fibroblast shows much higher elastic constants than the malignantly transformed fibroblasts. All the observed fibroblasts show that the elastic constants at the leading edge are lower than those from the cell body.

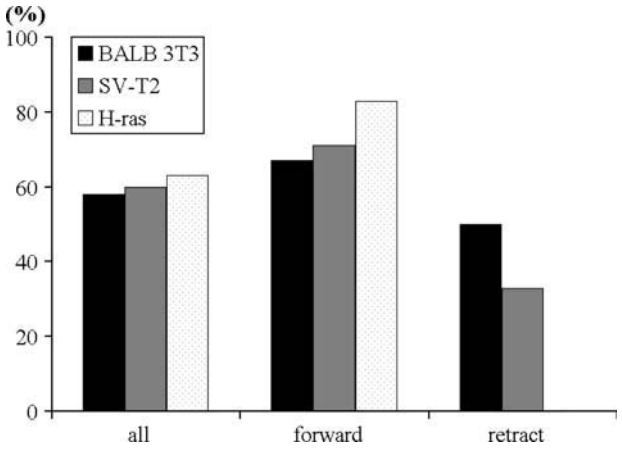

FIGURE 11 Percentage of the population for which the elastic constant, K, from the lamellipodium is lower than that from the cell body. The first group includes all the measured fibroblasts. The second and third groups include the advanced forward and retracted fibroblasts during the AFM measurements, respectively. More than 50% of the advanced forward fibroblasts show a lower elastic constant in the lamellipodium than in the cell body. On the contrary, a small portion of the retracted fibroblasts shows the lower elastic constants in the lamellipodium.

fibroblasts during a 30-min observation period. The arrows in Fig. 12 indicate the cells' moving direction. The malignantly transformed fibroblasts display distinct steps between the centroids as well as the longer net path lengths compared with the normal fibroblast.

Statistically, the three cell lines show a significant difference in the net path length and the mean speed, indicating an increase of both parameters in the malignantly transformed fibroblasts (see Fig. 13, *A* and *B*). The measured mean speeds are 6.1 ± 4.5 μm/h for BALB 3T3 fibroblasts, 13.1 ± 5.2 μm/h for SV-T2 fibroblasts, and 26.2 ± 11.5 μm/h for H-ras fibroblasts. The directionality, D, of the malignantly transformed fibroblasts was not significantly different from the normal fibroblasts (see Fig. 13 *C*). These results suggest that the increase in the net path length and the mean speed of the malignantly transformed fibroblasts is not due to an enhanced persistence of the moving direction. There is a report that an increase in the persistence of the moving direction can be a cause of an enhanced motility (39). However, the enhanced motility in malignantly transformed fibroblasts is not apparently caused by directionality, but rather is caused by an increase in the activity of the lamellipodium, A. In Fig. 13 *D*, the activity, A, significantly differs between H-ras transformed fibroblasts and BALB 3T3 fibroblasts. This finding indicates that malignant transformation significantly enhances cells' protrusive ability to extend and remodel their lamellipodia.

Actin fluorescence images

In fluorescence images showing the actin cytoskeleton, stress fibers are prominent and well developed in all of the observed cell lines. In a motile cell indicated through its polar

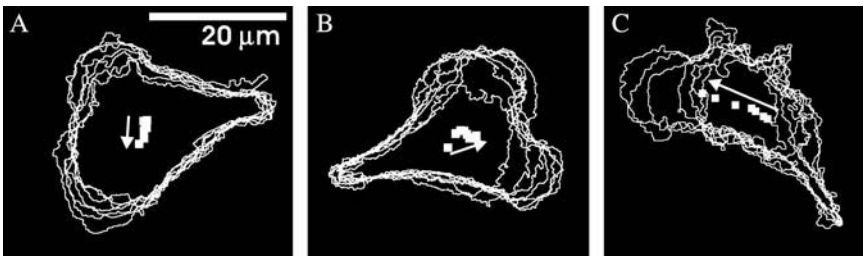

FIGURE 12 Perimeters and centroids obtained every 5 min for 30 min from a BALB 3T3 fibroblast (*A*), an SV-T2 fibroblast (*B*), and an H-ras transformed fibroblast (*C*). The arrows indicate the cell's moving direction.

directional appearance, fewer or no stress fibers were observed, whereas a resting cell shows very prominent stress fibers. Thus the presence of the stress fibers represents the state of a cell's activity rather than differences between cell lines. In Fig. 14, we present confocal images of actin filaments stained with rhodamine phalloidin from each cell of the three cell lines. In these images, the fluorescence intensity represents the average actin filament density. The actin filament density is low at the leading edge and increases toward the cell body. This is well depicted in the line profile of the intensity distribution. Along the dissected lines shown in Fig. 14, the fluorescent intensity of actin filaments is plotted as a function of the distance from the outside toward the nucleus. All of the line profiles show a decrease in the fluorescence intensity at the leading edges. This result is consistent with the lower elastic constant, K, measured in the leading edge.

DISCUSSION

Wide distributions of elastic constants, K, are observed from all three cell lines. This may be affected by the fact that the cells are not synchronized and may be at different stages of their cell cycle. Besides differences in the cell cycle, these deviations are mainly due to spatial variability of the viscoelastic properties throughout the cell. Theoretical calculations show that a cell's elastic modulus can differ by an order of magnitude depending on the degree of cross-linking of the actin filaments and its spatial distribution (42). For example,

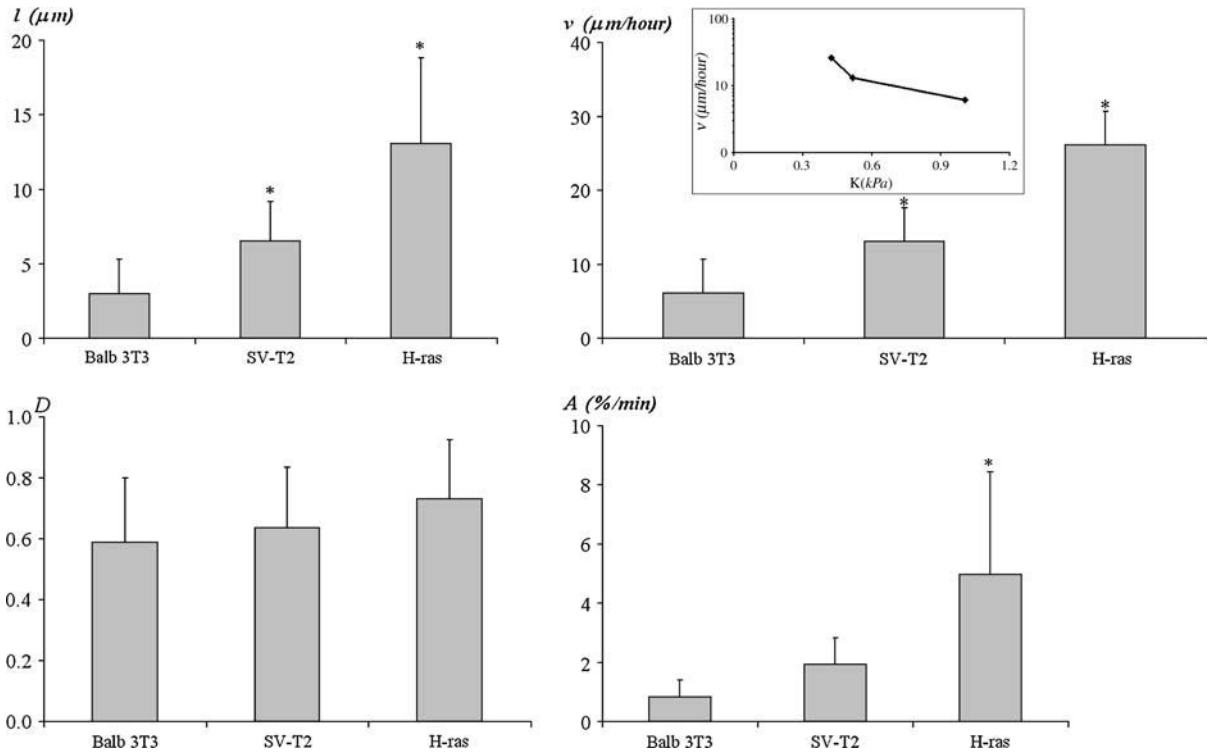

FIGURE 13 Quantities for the motility observed from the three cell lines. The numbers of studied cells are 19 for the BALB 3T3 fibroblasts, 13 for the SV-T2 fibroblasts, and 20 for the H-ras transformed fibroblasts. (*A*) The average net path length, l. All the observed cell lines display significant differences from each other ($p < 0.05$). (*B*) The mean speed, v. All the observed cell lines display significant differences from each other ($p < 0.05$). The inset plotted on a semilog scale shows the quantitative correlation between K and v from the three cell lines. (*C*) The average directionality, D. The three cell lines display no significant difference in the directionality. (*D*) The average activity, A. The H-ras transformed fibroblasts display a significant increase compared with the BALB 3T3 fibroblasts.

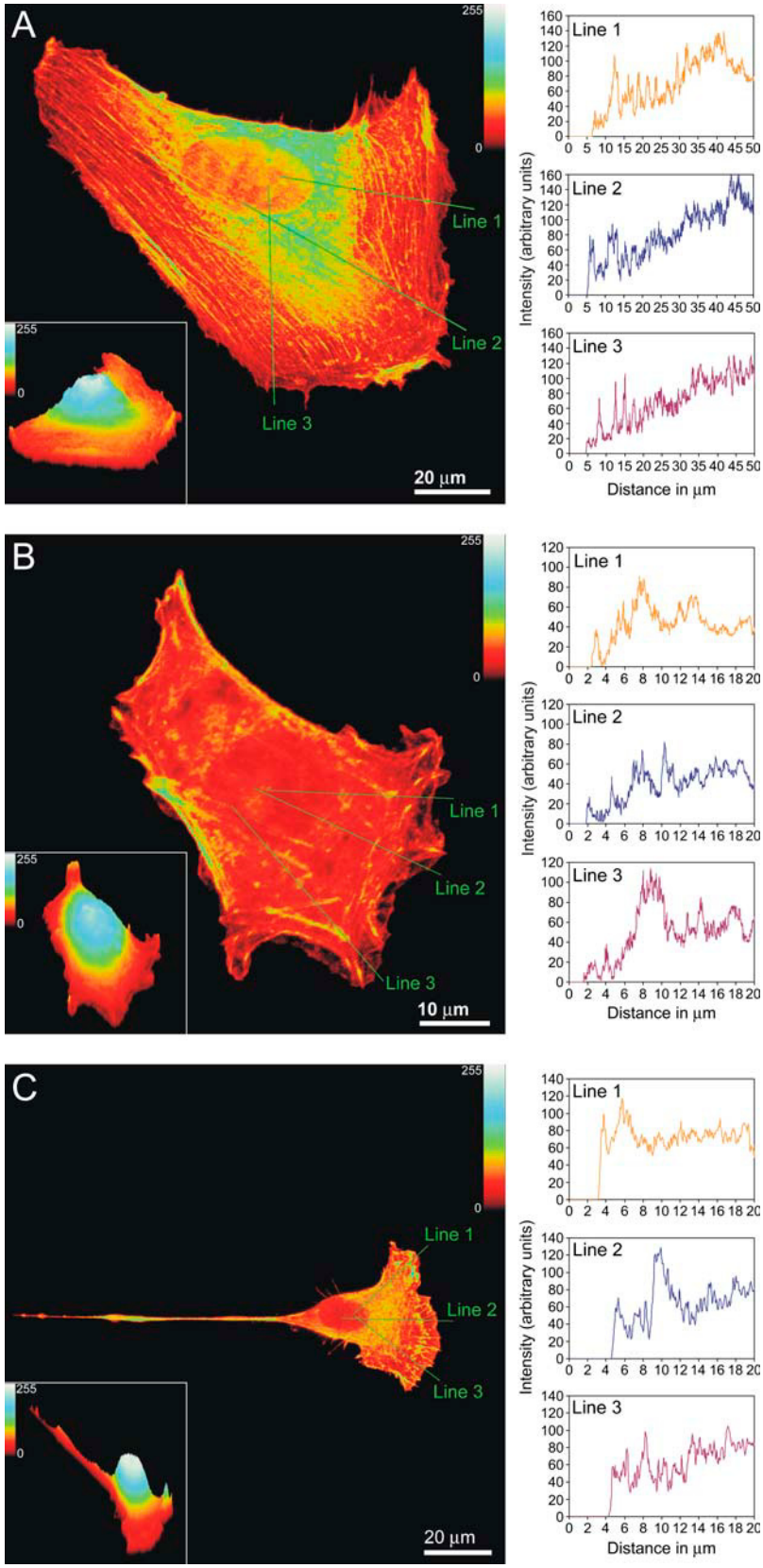

FIGURE 14 Actin fluorescence images of fibroblasts stained with rhodamine phalloidin. The inset of each image shows a three-dimensional confocal stack of the cell. The color gradients for the two-dimensional images indicate the fluorescence intensity, and those for the three-dimensional images indicate the height profile, the pixel count of the stacks. The line profiles obtained from the three dissected lines (*Line 1*, *Line 2*, and *Line 3*) are shown. The fluorescence intensities are plotted as a function of the distance from the outside toward the nucleus. (*A*) A BALB 3T3 fibroblast. (*B*) A SV-T2 fibroblast. (*C*) An H-ras transformed fibroblast.

the varying concentration of actin-binding proteins among cell lines affects the difference in the elastic moduli. Moreover, diverse spatial configurations of actin filaments in a cell—actin cortex underlying the plasma membrane and actin bundles, so-called stress fibers—modulate the elastic moduli. Thus, a wide distribution of the elastic constants reflects the heterogeneous nature of the actin cytoskeleton.

The malignant transformation results in a narrower distribution of elastic constants. This finding is consistent with reports about the increased disorder of the actin cytoskeleton in malignantly transformed cells (43,44). Moreover, our finding of the decrease in the elastic constants, K, observed in the malignantly transformed fibroblasts is consistent with previous studies on human bladder cells (45,46). Lekka et al. reported that the cancerous human bladder epithelial cell lines (Hu456, T24, and BC3726) have Young's moduli of $\sim$1 order of magnitude lower than normal bladder cell lines (Hu609 and HCV29) (46).

Our results also show that the malignant transformation enhances cells' motility. These results quantitatively agree with the previous investigations that have reported enhanced motility and migration speed for H-*ras* transformed fibroblasts (47–49).

Our measurements conclude that malignant transformation induces a decrease in viscoelastic properties and an increase in cell motility (see *inset* of Fig. 13 *B*). These results show a clear correlation between the enhanced motility and the decrease in viscoelastic constants. The loss constant, K'', has been shown to be a measure of the ability for a cell to transport cellular components while a cell moves. The lower loss constant results in faster transportation of the cellular components. Thus, the decrease in the loss constant, K'', as well as the storage constant, K', may contribute to the enhanced motility in malignantly transformed fibroblasts. However, the loss constant is constrained to explain the passive mechanism of cell motility through the transportation of cellular components. The storage constant plays a more substantial role in cell motility actively driven by the actin cytoskeleton. Since all cell lines display an elastic rubber plateau, the zero frequency elastic constants, K, equivalent to the storage constants, K', in the plateau regime were used for further statistical comparisons. We could not observe a recently reported scaling behavior characteristic for soft glasses (8,50,51). This is particularly interesting since this scaling law has been observed in AFM measurements (50,51). Our frequency-dependent measurements show that the ratio of K''/K', the hysteric damping coefficient, differs from the previously reported ratio (7,51). The deviations might be caused by different tip geometries.

In addition, the local profile of the elastic constants within a cell is an important characteristic for the applicability of the different models of cell motility. A high elastic constant, K, of the lamellipodium is a direct consequence of the dendritic nucleation model (18). This model considers highly cross-linked actin filaments in the lamellipodium as a major contributor to the cell's protrusive force. In contrast, the elastic ratchet model predicts a lower elastic constant for the lamellipodium (14). In this model, the most essential element of the cell's protrusion is considered to be the fluctuation of the soft free filament ends at the leading edge, which are supported by the rigid actin cytoskeleton in the main body. This model also predicts that softer networks in the lamellipodium can be achieved through lower concentrations of actin-binding proteins, which would cause less cross-linking and longer free filaments. Our spatial profile of the elastic constants shows the lower elastic constants in the lamellipodium as expected from the elastic ratchet model. This observed spatial profile of the elastic constants is consistent with our actin fluorescent images showing the low actin filament density at the leading edge. We would like to mention that we found a different behavior in fibroblasts on laminin-coated glass coverslips. Fibroblasts on the laminin-coated glass show a strong cortical actin rim unlike fibroblasts on glass. Thus results may differ for different substrates. We did not see any significant differences in the lamellipodial actin distribution of cells presenting a clear directionality between malignantly transformed fibroblasts and normal fibroblasts. This finding does not contradict the lower lamellipodial elastic constants, K, measured in malignantly transformed fibroblasts since these lower K could, for example, originate from a lower cross-linker density.

There is a report that *SV40*-transformed 3T3 cells display a reduced expression of the actin-binding protein, α-actinin (52). It is also known that the down regulation of α-actinin increases the cell motility and induces the malignant transformation of 3T3 fibroblasts (53). This line of investigation provides additional evidence of how the microscopic elastic Brownian ratchet model successfully explains the correlation between viscoelastic properties and motility. First, the concentration of actin-binding proteins is reduced for malignantly transformed fibroblasts. Second, this reduction produces a less cross-linked actin cortex and longer actin filaments in malignantly transformed fibroblasts. The less cross-linked actin cortex is responsible for both the decrease in viscoelastic moduli and the increase in cell motility.

However, an experiment done with human tumor cell lines show that a lack of actin-binding proteins results in impaired locomotion and cortical stability (54). In that study, the human tumor cell lines restored the translocational motility through the expression of actin-binding proteins. This implies that the absence of actin-binding proteins is the cause of the impaired motility. To reconcile these two contradictory results, we propose the need for a minimum concentration of actin-binding proteins to ensure a cell's normal motility although the lower concentration of actin-binding proteins can expedite the cell's protrusion.

Although many details of this proposed mechanism await further investigations, the microscopic elastic Brownian ratchet model can explain our mesoscopic findings that elastic moduli and motility are correlated. This mechanism proposes that

the enhanced thermal fluctuation in softer cells can expedite the protrusive motility mediated by the polymerization of the actin filaments.

We thank Dr. W. Frey for helpful discussions and Christopher Wieland for English correction.

J. Käs is supported by the Wolfgang-Paul prize of the Alexander von Humboldt Foundation. Additional funding was provided by the Integrative Graduate Education and Research Traineeship program administered by Dr. R. Richards-Kortum through a National Science Foundation grant (DGE-9870653).

REFERENCES

1. Borisy, G. G., and T. M. Svitkina. 2000. Actin machinery: pushing the envelope. *Curr. Opin. Cell Biol.* 12:104–112.
2. Stossel, T. P. 1993. On the crawling of animal cells. *Science.* 260:1086–1094.
3. Oliver, T., M. Dembo, and K. Jacobson. 1999. Separation of propulsive and adhesive traction stresses in locomoting Keratocytes. *J. Cell Biol.* 145:589–604.
4. Pantaloni, D., C. Le Clainche, and M. F. Carlier. 2001. Mechanism of actin-based motility. *Science.* 292:1502–1506.
5. Theriot, J. A., T. J. Mitchison, L. G. Tilney, and D. A. Portnoy. 1992. The rate of actin-based motility of intracellular *Listeria monocytogenes* equals the rate of actin polymerization. *Nature.* 357:257–260.
6. Fabry, B., G. N. Maksym, J. P. Butler, M. Glogauer, D. Navajas, and J. J. Fredberg. 2001. Scaling the microrheology of living cells. *Phys. Rev. Lett.* 87:148102.
7. Fabry, B., G. N. Maksym, J. P. Butler, M. Glogauer, D. Navajas, N. A. Taback, E. J. Millet, and J. J. Fredberg. Time scale and other invariants of integrative mechanical behavior in living cells. 2003. *Phys. Rev. E.* 68:041914.
8. Pasternak, C., and E. L. Elson. 1985. Lymphocyte mechanical response triggered by cross-linking surface receptors. *J. Cell Biol.* 100:860–872.
9. Elson, E. L. 1988. Cellular mechanics as an indicator of cytoskeletal structure and function. *Annu. Rev. Biophys. Biophys. Chem.* 17:397–430.
10. Rotsch, C., K. Jacobson, J. Condeelis, and M. Radmacher. 2001. EGF-stimulated lamellipod extension in adenocarcinoma cells. *Ultramicroscopy.* 86:97–106.
11. Fukui, Y. 2002. Mechanistics of amoeboid locomotion: signal to forces. *Cell Biol. Int.* 26:933–944.
12. Gerbal, F., C. Paul, Y. Rabin, and J. Prost. 2000. An elastic analysis of *Listeria monocytogenes* propulsion. *Biophys. J.* 79:2259–2275.
13. Peskin, C. S., G. M. Odell, and G. F. Oster. 1993. Cellular motions and thermal fluctuations: the Brownian ratchet. *Biophys. J.* 65:316–324.
14. Mogilner, A., and G. Oster. 1996. Cell motility driven by actin polymerization. *Biophys. J.* 71:3030–3045.
15. Goldberg, M., and J. Theriot. 1995. Shigella flexneri surface protein IcsA is sufficient to direct actin-based motility. *Proc. Natl. Acad. Sci. USA.* 92:6572–6576.
16. Small, J. V. 1994. Lamellipodia architecture: actin filament turnover and the lateral flow of actin filaments during motility. *Semin. Cell Biol.* 5:157–163.
17. Marcy, Y., J. Prost, M.-F. Carlier, and C. Sykes. 2004. Forces generated during actin-based propulsion: a direct measurement by micromanipulation. *Proc. Natl. Acad. Sci. USA.* 101:5992–5997.
18. Mullins, R. D., J. A. Heuser, and T. D. Pollard. 1998. The interaction of Arp2/3 complex with actin: nucleation, high affinity pointed end capping, and formation of branching networks of filaments. *Proc. Natl. Acad. Sci. USA.* 95:6181–6186.
19. Svitkina, T. M., and G. G. Borisy. 1999. Arp2/3 complex and actin depolymerizing factor/cofilin in dendritic organization and treadmilling of actin filament array in lamellipodia. *J. Cell Biol.* 145:1009–1026.
20. De Lozanne, A., and J. A. Spudich. 1987. Disruption of the *Dictyostelium* myosin heavy chain gene by homologous recombination. *Science.* 236:1086–1091.
21. Knecht, D. A., and W. F. Loomis. 1987. Antisense RNA inactivation of myosin heavy chain gene expression in *Dictyostelium discoideum.* *Science.* 236:1081–1086.
22. Titus, M. A., D. Wessels, J. A. Spudich, and D. Soll. 1993. The unconventional myosin encoded by the myoA gene plays a role in *Dictyostelium* motility. *Mol. Biol. Cell.* 4:233–246.
23. Wessels, D., M. Titus, and D. R. Soll. 1996. A *Dictyostelium* myosin 1 plays a crucial role in regulating the frequency of pseudopods formed on the substratum. *Cell Motil. Cytoskeleton.* 33:64–79.
24. Wottawah, F., S. Schinkinger, B. Lincoln, R. Ananthakrishnan, M. Romeyke, J. Guck, and J. Käs. 2005. Optical rheology of biological cells. *Phys. Rev. Lett.* 94:098103.
25. Guck, J., S. Schinkinger, B. Lincoln, F. Wottawah, S. Ebert, M. Romeyke, D. Lenz, H. M. Erickson, R. Ananthakrishnan, D. Mitchell, J. Käs, S. Ulvick, and C. Bilby. 2005. Optical deformability as an inherent cell marker for testing malignant transformation and metastatic competence. *Biophys. J.* 88:3689–3698.
26. Bos, T. J., P. Margiotta, L. Bush, and W. Wasilenko. 1999. Enhanced cell motility and invasion of chicken embryo fibroblasts in response to *Jun* over-expression. *Int. J. Cancer.* 81:404–410.
27. Hill, S. A., S. Wilson, and A. F. Chambers. 1988. Clonal heterogeneity, experimental metastatic ability, and p21 expression in H-*ras*-transformed NIH 3T3 cells. *J. Natl. Cancer Inst.* 80:484–490.
28. Mahaffy, R. E., C. K. Shih, F. C. MacKintosh, and J. Käs. 2000. Scanning probe-based frequency-dependent microrheology of polymer gels and biological cells. *Phys. Rev. Lett.* 85:880–883.
29. Amblard, F., A. C. Maggs, B. Yurke, A. N. Pargellis, and S. Leibler. 1996. Subdiffusion and anomalous local viscoelasticity in actin networks. *Phys. Rev. Lett.* 77:4470–4473.
30. Petersen, N. O., W. B. McConnaughey, and E. L. Elson. 1982. Dependence of locally measured cellular deformability on position on the cell, temperature and cytochalasin B. *Proc. Natl. Acad. Sci. USA.* 79:5327–5331.
31. Rotsch, C., K. Jacobson, and M. Radmacher. 1999. Dimensional and mechanical dynamics of active and stable edges in motile fibroblasts investigated by using atomic force microscopy. *Proc. Natl. Acad. Sci. USA.* 96:921–926.
32. Yamada, S., D. Wirtz, and S. C. Kuo. 2000. Mechanics of living cells measured by laser tracking microrheology. *Biophys. J.* 78:1736–1747.
33. Ziemann, F., J. Rädler, and E. Sackmann. 1994. Local measurements of viscoelastic moduli of entangled actin networks using an oscillating magnetic bead micro-rheometer. *Biophys. J.* 66:2210–2216.
34. Mahaffy, R. E., S. Park, E. Gerde, J. Käs, and C. K. Shih. 2004. Quantitative analysis of the viscoelastic properties in thin regions of fibroblasts using AFM. *Biophys. J.* 86:1777–1793.
35. Chen, W. T. 1971. Computation of stresses and displacements in a layered elastic medium. *Int. J. Eng. Sci.* 9:775–800.
36. Chen, W. T., and P. A. Engel. 1972. Impact and contact stress analysis in multilayer media. *Int. J. Solids Struct.* 8:1257–1281.
37. Tu, Y.-O., and D. C. Gazis. 1964. The contact problem of a plate pressed between two spheres. *J. Appl. Mech.* 31:659–666.
38. Soll, D. R. 1995. The use of computers in understanding how animal cells crawl. *Int. Rev. Cytol.* 163:43–104.
39. Shestakova, E. A., R. H. Singer, and J. Condeelis. 2001. The physiological significance of β-actin mRNA localization in determining cell polarity and directional motility. *Proc. Natl. Acad. Sci. USA.* 98:7045–7050.
40. Tortonese, M., and M. Kirk. 1997. Characterization of application specific probes for SPMs. *Micromachining and Imaging SPIE.* 3009: 53–60.

41. Butt, H. J., and M. Jaschke. 1995. Calculation of thermal noise in atomic force microscopy. *Nanotechnology*. 6:1–7.

42. Ananthakrishnan, R., J. Guck, F. Wottawah, S. Schinkinger, B. Lincoln, M. Romyeke, and J. Käs. 2005. Modeling the structural response of an eukaryotic cell in the optical stretcher. *Curr. Sci.* 88:1434–1440.

43. Koffer, A., M. Daridan, and G. Clarke. 1985. Regulation of the microfilament system in normal and polyoma virus transformed cultured (BHK) cells. *Tissue Cell*. 17:147–159.

44. Takahashi, K., V. I. Heing, J. L. Junker, N. H. Colburn, and J. M. Rice. 1986. Role of cytoskeleton changes and expression of the H-ras oncogene during promotion of neoplastic transformation in mouse epidermal JB6 cells. *Cancer Res*. 46:5923–5932.

45. Ward, K. A., W.-I. Li, S. Zimmer, and T. Davis. 1991. Viscoelastic properties of transformed cells: role in tumor cell progression and metastasis formation. *Biorheology*. 28:301–313.

46. Lekka, M., P. Laidler, D. Gil, J. Lekki, Z. Stachura, and A. Z. Hrynkiewicz. 1999. Elasticity of normal and cancerous human bladder cells studied by scanning force microscopy. *Eur. Biophys. J*. 28:312–316.

47. Varani, J., S. E. Fligiel, and B. Wilson. 1986. Motility of *rasH* oncogene transformed NIH-3T3 cells. *Invasion Metastasis*. 6:335–346.

48. Shelden, E. 1999. Major role of active extension in the formation of processes by *ras*-transformed fibroblasts. *Cell Motil. Cytoskeleton*. 41:12–26.

49. Sahai, E., M. F. Olsen, and C. J. Marshall. 2001. Cross-talk between *Fas* and *Rho* signaling pathways in transformation favors proliferation and increased motility. *EMBO J*. 20:755–766.

50. Shroff, S. G., D. R. Saner, and R. Lal. 1995. Dynamic micromechanical properties of cultured rat atrial myocytes measured by atomic force microscopy. *Am. J. Physiol.* 269:C286–C292.

51. Alcaraz, J., L. Buscemi, M. Grabulosa, X. Trepat, B. Fabry, R. Farre, and D. Navajas. 2003. Microrheology of human lung epithelian cells measured by atomic force microscopy. *Biophys. J*. 84:2071–2079.

52. Gluck, U., D. J. Kwiatkowski, and A. Ben-Ze'ev. 1993. Suppression of tumorigenicity in simian virus 40-transformed 3T3 cells transfected with α-actinin cDNA. *Proc. Natl. Acad. Sci. USA*. 90:383–387.

53. Gluck, U., and A. Ben-Ze'ev. 1994. Modulation of α-actinin levels affects cell motility and confers tumorigenicity on 3T3 cells. *J. Cell Sci.* 107:1773–1782.

54. Cunningham, C. C., J. B. Corlin, D. J. Kwiatkowski, J. H. Hartwig, P. A. Janmey, H. R. Byers, and T. P. Stossel. 1992. Actin-binding protein requirement for cortical stability and efficient locomotion. *Science*. 255:325–327.